Catalysis Science & Technology

PAPER

View Article Online
View Journal

Cite this: DOI: 10.1039/c6cy02572b

Hexagonal $Zn_{1-x}Cd_xS$ ($0.2 \leq x \leq 1$) solid solution photocatalysts for H_2 generation from water†

Zongwei Mei,[a] Mingjian Zhang,[a] Julian Schneider,[b] Wei Wang,[c] Ning Zhang,[d] Yantao Su,[a] Bingkun Chen,[b] Shufeng Wang,[c] Andrey L. Rogach[b] and Feng Pan*[a]

Received 9th December 2016,
Accepted 24th January 2017

DOI: 10.1039/c6cy02572b

rsc.li/catalysis

A series of hexagonal $Zn_{1-x}Cd_xS$ photocatalysts with variable composition ($0.2 \leq x \leq 1$) is synthesized by a solvothermal method. XPS spectra of Zn 2p and Cd 3d regularly shift upon changing the composition of $Zn_{1-x}Cd_xS$ samples, due to the difference in the Mulliken atomic charges of Zn, Cd, and S. The photocatalytic activity of the samples for H_2 evolution from water was tested under visible-light irradiation ($\lambda \geq 420$ nm) without a cocatalyst; the $Zn_{0.4}Cd_{0.6}S$ sample exhibited the highest photocatalytic H_2 evolution rate, which was about 81 mL h^{-1} g^{-1}. Under irradiation with a 368 nm LED, the H_2 evolution rate decreased with increasing Cd fraction in the $Zn_{1-x}Cd_xS$ solid solution. By comparing the crystallinity, surface area, valence/conduction band positions, absorption spectra and fluorescence lifetimes, we conclude that the photocatalytic activity is related to the balance between the absolute positions of the valence/conduction bands and light absorption ability of the $Zn_{1-x}Cd_xS$ photocatalysts.

1. Introduction

Photocatalytic H_2 generation from water is one of the attractive ways for the utilization of green solar energy.[1–3] Highly active and visible-light-sensitive photocatalysts are vital to the practical application of this approach.[4,5] Metal sulfides have been considered as possible photocatalysts;[6,7] in particular $Zn_{1-x}Cd_xS$ solid solutions have an advantage of a continuously adjustable band gap and have demonstrated high photocatalytic activity for H_2 evolution from water under visible-light irradiation even without any cocatalysts,[8] which has been superior to bare CdS.[9] $Zn_{1-x}Cd_xS$ powders and films have been synthesized for photocatalytic water splitting;[10–12] especially, $Zn_{1-x}Cd_xS$ powders possessing nano-twin structures with a twin-boundary-dependent potential were reported to prevent the recombination of photo-induced carriers.[13] For $Cd_{1-x}Zn_xS$ ($0 \leq x \leq 1$) solid solutions, the crystal structure changes from hexagonal to cubic with increasing x, with $Zn_{0.5}Cd_{0.5}S$ and $Zn_{0.81}Cd_{0.19}S$ compositions displaying the highest photocatalytic activity.[14–16] Navarro *et al.* reported a hexagonal $Cd_{1-x}Zn_xS$ microstructure with $0.2 < x < 0.35$, where the sample with $x = 0.3$ showed the highest photocatalytic activity for water splitting.[17] Wang *et al.* fabricated $Cd_{1-x}Zn_xS$ nanocrystals with a cubic zinc-blende phase and found that $Cd_{0.44}Zn_{0.56}S$ performed best as the photocatalyst for H_2 evolution.[18] Xu and Chan developed a series of cubic zinc-blende $Zn_{1-x}Cd_xS$ ($0 \leq x \leq 1$) with $Zn_{0.80}Cd_{0.20}S$, $Zn_{0.5}Cd_{0.5}S$ and $Zn_{0.4}Cd_{0.6}S$ exhibiting high H_2 evolution rates.[19,20]

The photocatalytic activity of $Zn_{1-x}Cd_xS$ can be further improved by coupling to other compounds, such as MoS_2, graphene, and reduced graphene oxide.[21–24] Some other metal sulfides such as CdS and NiS were also proved to be efficient cocatalysts which are able to improve the photocatalytic H_2 evolution rate from $Zn_{1-x}Cd_xS$.[25,26] Additionally, transition metal elements as dopants were useful to enhance the photocatalytic activity of $Zn_{1-x}Cd_xS$.[3,27,28]

Although Li *et al.* have studied the photocatalytic performance of cubic or hexagonal $Cd_{1-x}Zn_xS$ particles for water splitting, it is important to be able to produce $Zn_{1-x}Cd_xS$ solid solutions of a single controllable phase (cubic *versus* hexagonal) with variable composition (x) and carry out more detailed study about the photocatalytic activities. In this report, we demonstrate a successful synthesis of powdered hexagonal $Zn_{1-x}Cd_xS$ photocatalysts with x varying from 0 to 1 and show that their photocatalytic activity in terms of H_2 evolution from water is related to the balance between the absolute positions

---

[a] School of Advanced Materials, Peking University Shenzhen Graduate School, 2199 Lishui Road, Shenzhen 518055, China. E-mail: panfeng@pkusz.edu.cn
[b] Department of Physics and Materials Science & Center for Functional Photonics (CFP), City University of Hong Kong, Hong Kong S. A. R, China
[c] State Key Laboratory for Artificial Microstructure and Mesoscopic Physics, Department of Physics, Peking University, Beijing 100871, China
[d] School of Materials Science and Engineering, Central South University, Changsha, Hunan 410083, China

† Electronic supplementary information (ESI) available. See DOI: 10.1039/c6cy02572b

of the valence/conduction bands and the light absorption ability.

2. Experimental

2.1. Materials

Precursor materials include $Zn(NO_3)_2\cdot 6H_2O$ (purity 99.99%), $Cd(CH_3COO)_2\cdot 2H_2O$ (purity 99.99%), ethylenediamine (analytical reagent), and $Na_2S\cdot 9H_2O$ (purity 99.99%), all purchased from Aladdin Industrial Corporation, China.

2.2. Synthesis of $Zn_{1-x}Cd_xS$ solid solution photocatalysts

In a typical process, $3(1 - x)$ mmol of $Zn(NO_3)_2\cdot 6H_2O$ and $3x$ mmol of $Cd(CH_3COO)_2\cdot 2H_2O$ were dissolved in 20 mL of distilled water to form a clear solution. 80 mL of ethylenediamine was added, followed by addition of $Na_2S\cdot 9H_2O$ (4 mmol) solution dissolved in 20 mL of distilled water. The mixture was transferred into a Teflon lined (180 mL capacity) sealed stainless steel autoclave and heated at 200 °C for 24 h. The system was cooled to room temperature, and the products were cleaned three times using distilled water and ethanol and dried into powders in a vacuum oven at 60 °C for 12 h.

3. Characterization

The atomic ratio in the $Zn_{1-x}Cd_xS$ samples was estimated by inductively coupled plasma-atomic emission spectroscopy (ICP-AES, JY2000-2). The crystal structure of the photocatalysts was characterized by X-ray diffraction (XRD) using a D8 Advance (Germany) machine with Cu Kα radiation (λ = 0.15406 nm). Transmission electron microscopy (TEM) and high-resolution TEM (HRTEM) images were obtained using a TEI Tecnai G2 F30 machine at 300 kV. The Brunauer–Emmett–Teller (BET) surface area was characterized by nitrogen adsorption at 77 K using an accelerated surface area and porosimetry system (ASAP 2020 HD88). UV-vis diffuse reflectance spectra of the powdered samples were obtained using a Tu-1901 UV-vis spectrophotometer. The photoluminescence (PL) spectra and PL decays were recorded on an FLS 9802 fluorescence spectrometer. X-ray photoelectron spectroscopy (XPS) was carried out using an ESCALAB 250Xi machine with Al Kα radiation; all the XPS spectra were calibrated by the graphitic signal at 284.8 eV.

4. DFT calculation

Density functional theory (DFT) calculations were performed using the CASTEP Package. The Perdew–Burke–Ernzerhof (PBE) functional of the generalized gradient approximation (GGA) was used as the exchange-correlation functional.[29,30] The ultrasoft pseudopotential was used to describe the interaction between the valence electrons and the ionic core. Based on the XRD patterns, all $Zn_{1-x}Cd_xS$ solid solutions crystallized in the *P*63*mc* space group as shown in the Results and discussion section. We thus chose a hexagonal ZnS supercell (5 × 1 × 2, containing 20 Zn atoms and 20 S atoms) as the initial model for $Zn_{1-x}Cd_xS$ (x = 0). All other models were constructed by using a defined amount of Cd atoms to replace Zn atoms based on the ZnS supercell as explicitly presented in Fig. S1, ESI.† The geometry optimizations were performed using the plane-wave projector-augmented wave method with a cutoff energy of 310 eV. The Monkhorst–Pack *k*-point mesh was set as 1 × 4 × 1, and the self-consistent field was 1×10^{-5} eV per atom. The atomic relaxations were conducted until the residual force was smaller than 0.03 eV $Å^{-1}$. Finally, the electronic structures and population analysis results of the optimized supercells were obtained.

5. Photocatalytic tests

The photocatalytic activity tests were carried out in a quartz-cell reactor with a side window, which was connected to a closed gas-circulation system. In each test, 0.1 g of the powdered photocatalyst was added into the reactor containing 300 ml of Na_2S (0.35 M)/Na_2SO_3 (0.25 M) aqueous solution. Visible light ($\lambda \geq 420$ nm) was generated by a 300 W Xe lamp equipped with a UV cut-off filter (UVCUT 420, AU-LIGHT Co. Ltd., China). Because of the poor absorption of ZnS and $Zn_{0.9}Cd_{0.1}S$ to the 368 nm LED (not shown in this work), we tested the samples from $Zn_{0.8}Cd_{0.2}S$ to CdS. The amount of evolved H_2 has been determined using an online gas chromatograph (GC7900(T), TECHCOMP, China) equipped with a thermal conductivity detector.

6. Results and discussion

Table 1 shows the ICP-AES characterization data of all $Zn_{1-x}Cd_xS$ samples, from which the respective structural formulae have been derived. Based on the tested concentration (CC, mg L^{-1}), the content of Cd (value of x) is calculated and varies from 0.2 to 0.9, which is in accordance with the ratios of Zn to Cd used for the synthesis of the samples. Fig. 1 shows the XRD patterns of the $Zn_{1-x}Cd_xS$ powdered samples, comparing them to CdS synthesized in a similar way. All the

Table 1 ICP-AES characterization of the $Zn_{1-x}Cd_xS$ ($0.2 \leq x \leq 1$) samples

	Element	CC (mg L^{-1})	Zn : Cd	Structural formula
Sample 1	Zn	29.27	3.943	$Zn_{0.80}Cd_{0.20}S$
	Cd	12.76		
Sample 2	Zn	26.23	2.325	$Zn_{0.70}Cd_{0.30}S$
	Cd	19.39		
Sample 3	Zn	30.58	1.479	$Zn_{0.60}Cd_{0.40}S$
	Cd	35.54		
Sample 4	Zn	18.42	0.939	$Zn_{0.48}Cd_{0.52}S$
	Cd	33.71		
Sample 5	Zn	16.23	0.620	$Zn_{0.38}Cd_{0.62}S$
	Cd	45.01		
Sample 6	Zn	9.27	0.413	$Zn_{0.29}Cd_{0.71}S$
	Cd	38.57		
Sample 7	Zn	8.08	0.231	$Zn_{0.19}Cd_{0.81}S$
	Cd	60.19		
Sample 8	Zn	3.77	0.105	$Zn_{0.10}Cd_{0.90}S$
	Cd	61.65		

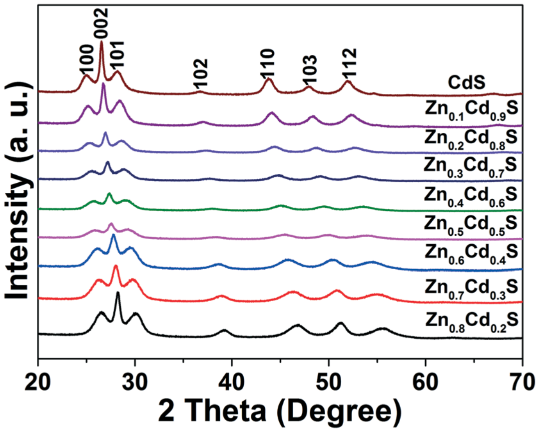

Fig. 1 XRD patterns of the powdered $Zn_{1-x}Cd_xS$ samples.

samples can be indexed to the hexagonal structure; the peaks gradually shift to those of the hexagonal CdS (*P*63*mc*, JCPDS: PDF-41-1049) when the amount of Cd increases, confirming that samples are solid solutions between ZnS and CdS. Due to the poorer crystallinity of $Zn_{0.4}Cd_{0.6}S$ and $Zn_{0.5}Cd_{0.5}S$, their (102) diffraction peaks are not obvious in comparison with others. The XRD patterns of hexagonal ZnS and $Zn_{0.9}Cd_{0.1}S$ are shown in Fig. S2.† Fig. 2 shows representative TEM and HRTEM images of the $Zn_{1-x}Cd_xS$ samples, which are composed of quasi-spherical nanoparticles for the $Zn_{0.8}Cd_{0.2}S$ sample and elongated nanorods for all other samples (see Fig. S3†). The interplanar spacings (Fig. 2 and S3†) vary from 0.25 nm for the (102) plane for the $Zn_{0.8}Cd_{0.2}S$ sample with the lowest Cd content to 0.34 nm for the (002) plane for pure CdS.

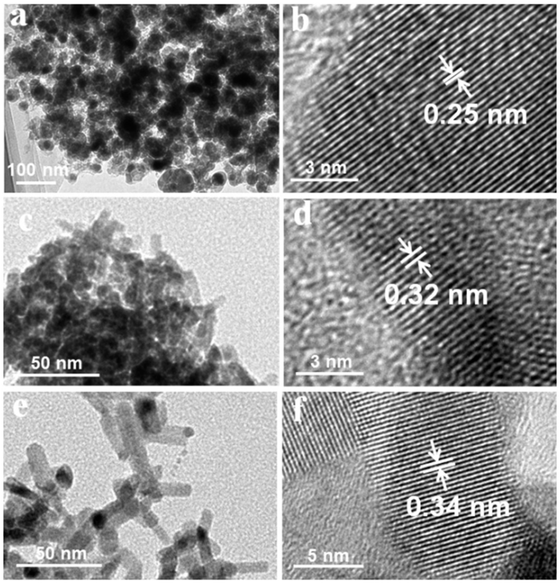

Fig. 2 Representative TEM (left column) and HRTEM (right column) images of (a and b) $Zn_{0.8}Cd_{0.2}S$, (c and d) $Zn_{0.4}Cd_{0.6}S$, and (e and f) CdS, respectively.

Fig. 3 shows the XPS spectra of Zn 2p, Cd 3d, and S 2p of the $Zn_{1-x}Cd_xS$ samples. For ZnS, the spectra of Zn 2p are located at 1022.5 eV for Zn $2p_{3/2}$ and 1045.5 eV for Zn $2p_{1/2}$ (Fig. 3a). For CdS, the spectra of Cd 3d are located at 405.5 eV for Cd $3d_{5/2}$ and 412.3 eV for Cd $3d_{1/2}$. The spectra of S 2p for both ZnS (fitted as shown in Fig. 3e) and CdS are both at 161.9 eV and 163.1 eV for S $2p_{3/2}$ and S $2p_{1/2}$, respectively. The spectra values of Zn 2p, Cd 3d and S 2p are in agreement with those of the reported ZnS and CdS.[14,31] The Zn 2p and Cd 3d spectra of $Zn_{1-x}Cd_xS$ solid solutions shift in comparison with those of ZnS and CdS according to the spectra of Zn $2p_{3/2}$ (Fig. 3b) and Cd $3d_{5/2}$ (Fig. 3d). It can also be observed that Zn $2p_{3/2}$ has an almost similar binding energy for a variety of samples from $Zn_{0.8}Cd_{0.2}S$ to $Zn_{0.1}Cd_{0.9}S$. However, the binding energy of Cd $3d_{5/2}$ becomes larger from $Zn_{0.8}Cd_{0.2}S$ to $Zn_{0.1}Cd_{0.9}S$. The S 2p spectrum of $Zn_{1-x}Cd_xS$ solid solutions shows a similar binding energy to those of ZnS and CdS as shown in Fig. 3e and S4.†

In order to explain such shifts of XPS spectra of Zn 2p and Cd 3d, theoretical calculations have been performed to determine the Mulliken atomic charges of Zn and Cd elements in the $Zn_{1-x}Cd_xS$ solid solutions with varying x (Table 2). In comparison with ZnS, the Mulliken atomic charges of Zn becomes larger for $Zn_{1-x}Cd_xS$ ($0.2 \leq x \leq 0.9$), which results in a smaller binding energy than that of ZnS, while the smaller Mulliken atomic charges of Cd compared with CdS causes a larger binding energy of $Zn_{1-x}Cd_xS$ than that of CdS. For $Zn_{1-x}Cd_xS$ solid solutions, the difference in Mulliken atomic charges between Zn and S becomes larger from $Zn_{0.8}Cd_{0.2}S$ to $Zn_{0.1}Cd_{0.9}S$. Additionally, the first ionization energy of Zn

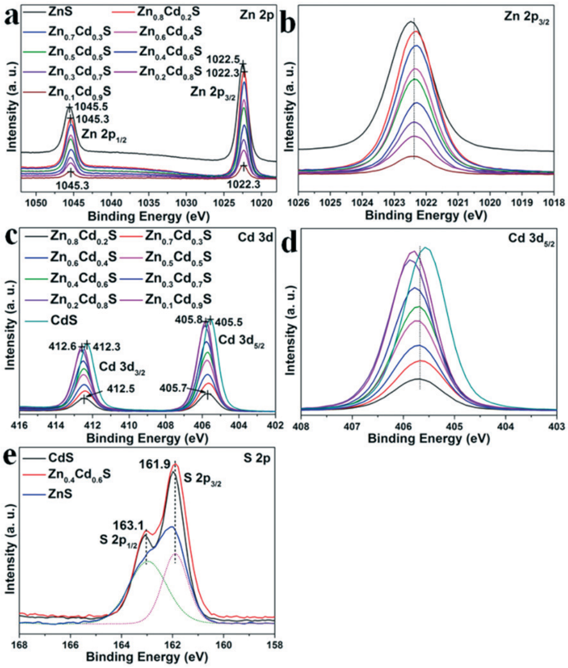

Fig. 3 XPS spectra of (a) Zn 2p, (b) Zn $2p_{3/2}$, (c) Cd 3d, and (d) Cd $3d_{5/2}$ of a series of $Zn_{1-x}Cd_xS$ ($0.2 \leq x \leq 1$) samples. Frame (e) compares the S 2p XPS spectra of CdS, $Zn_{0.4}Cd_{0.6}S$, and ZnS.

Table 2 Mulliken atomic charges and BET surface areas of the powdered $Zn_{1-x}Cd_xS$, ZnS and CdS samples

Sample	Mulliken atomic charges			Surface area ($m^2\ g^{-1}$)
	Zn	Cd	S	
ZnS	0.49		−0.49	—
$Zn_{0.8}Cd_{0.2}S$	0.50	0.55	−0.51	141
$Zn_{0.7}Cd_{0.3}S$	0.51	0.54	−0.52	155
$Zn_{0.6}Cd_{0.4}S$	0.53	0.54	−0.53	147
$Zn_{0.5}Cd_{0.5}S$	0.55	0.54	−0.55	144
$Zn_{0.4}Cd_{0.6}S$	0.55	0.56	−0.56	137
$Zn_{0.3}Cd_{0.7}S$	0.54	0.58	−0.57	127
$Zn_{0.2}Cd_{0.8}S$	0.54	0.59	−0.58	117
$Zn_{0.1}Cd_{0.9}S$	0.54	0.59	−0.59	99
CdS		0.60	−0.60	97

(906.4 kJ mol^{-1}) is larger than that of Cd (867.8 kJ mol^{-1}). Thus, Cd must lose more electrons than Zn with increasing Cd fraction in $Zn_{1-x}Cd_xS$ solid solutions, which explains why the Zn 2p XPS spectrum shows an almost similar binding energy, while the Cd 3d spectra gradually shift to larger energies from $Zn_{0.8}Cd_{0.2}S$ to $Zn_{0.1}Cd_{0.9}S$.

Aside from the Mulliken atomic charges, Table 2 also presents the BET surface areas of the $Zn_{1-x}Cd_xS$ samples, which exhibit a general trend of a gradual decrease with an increase in the Cd content. The largest surface area is about 155 $m^2\ g^{-1}$ for $Zn_{0.70}Cd_{0.30}S$, and the smallest one is about 97 $m^2\ g^{-1}$ for CdS. The typical N_2 adsorption–desorption isotherms of $Zn_{0.8}Cd_{0.2}S$ nanoparticles and $Zn_{0.4}Cd_{0.6}S$ nanorods are displayed in Fig. S5.†

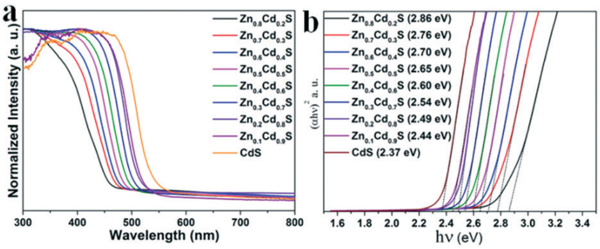

Fig. 4 (a) UV-vis diffuse reflectance spectra and (b) the $(\alpha h\nu)^2$–$h\nu$ plots of the powdered $Zn_{1-x}Cd_xS$ ($0.2 \le x \le 1$) samples.

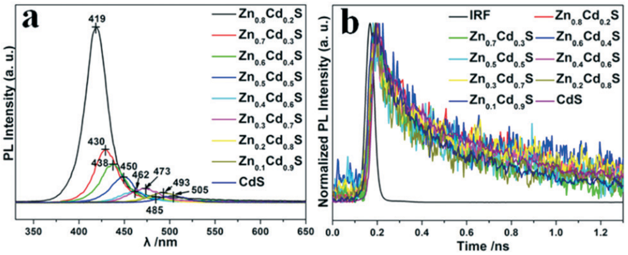

Fig. 5 (a) PL spectra obtained at 320 nm excitation and (b) normalized PL decay curves of the $Zn_{1-x}Cd_xS$ ($0.2 \le x \le 1$) samples; IRF stands for the instrument response function.

Fig. 4a shows the UV-vis diffuse reflectance spectra of the powdered $Zn_{1-x}Cd_xS$ ($0.2 \le x \le 1$) samples, which gradually shift to longer wavelengths when the amount of Cd is increased. The band gaps of the $Zn_{1-x}Cd_xS$ ($0.2 \le x \le 1$) samples have been estimated from these spectra based on the Kubelka–Munk method,[14] as shown in Fig. 4b; they vary from 2.86 eV for $Zn_{0.8}Cd_{0.2}S$ to 2.37 eV for CdS. These changes are in accordance with the trends seen in the PL spectra of the $Zn_{1-x}Cd_xS$ samples, which are presented in Fig. 5a. The emission peak position shifts from 419 nm for $Zn_{0.8}Cd_{0.2}S$ to 505 nm for CdS. At the same time, the fluorescence intensity is strongly quenched with increasing molar fraction of Cd. Fig. 5b shows the PL decay curves of the $Zn_{1-x}Cd_xS$ samples obtained at 320 nm laser excitation. All samples show multiexponential decays with average fluorescence lifetimes in the range of 1 ns. Since the average lifetimes do not change in solid solutions with a higher Cd content, we note from the lower PL intensities an increase in non-radiative decay pathways, which compete with fluorescence. The absolute position of the conduction bands for $Zn_{0.8}Cd_{0.2}S$, $Zn_{0.4}Cd_{0.6}S$, and CdS at zero charge (pH_{zpc}) can be evaluated by the following equation:[7]

$$E^0_{CB} = X - E^c - 1/2E_g$$

where X is the absolute electronegativity of the semiconductor, which shows the geometric mean of the absolute electronegativity of the constituent atoms, and is defined as the arithmetic mean of the atomic electron affinity and the first ionization energy; E^c is the energy of free electrons on the hydrogen scale (∽4.5 eV); and E_g is the band gap of the semiconductor. The calculated values of X are 5.25 eV, 5.22 eV, and 5.19 eV for $Zn_{0.8}Cd_{0.2}S$, $Zn_{0.4}Cd_{0.6}S$, and CdS, respectively. Based on the above equation and the calculated band gaps, the conduction band edges of $Zn_{0.8}Cd_{0.2}S$ (E_g = 2.86 eV), $Zn_{0.4}Cd_{0.6}S$ (E_g = 2.60 eV), and CdS (E_g = 2.37 eV) are about −0.68 eV, −0.58 eV, and −0.50 eV, respectively. And their valence band edges are about 2.18 eV, 2.02 eV, and 1.87 eV, respectively.

Fig. 6a shows the average H_2 generation rate of $Zn_{1-x}Cd_xS$ powders in terms of a half-reaction of photocatalytic water splitting, which has been performed under visible-light irradiation ($\lambda \ge 420$ nm) without a cocatalyst in a closed gas-circulation system. The photocatalysts (0.1 g) were dispersed in water in the presence of Na_2S (0.35 M)/Na_2SO_3 (0.25 M) as sacrificial hole scavengers and tested for 8 h. The evolved H_2 amount was detected by online gas chromatography. The photocatalytic activity goes through a maximum as x increases (Fig. 6a), with the $Zn_{0.4}Cd_{0.6}S$ sample showing the best performance (the H_2 evolution rate is 81 mL $h^{-1}\ g^{-1}$ or 3.6 mmol $h^{-1}\ g^{-1}$). We further checked the photocatalytic performance of $Zn_{1-x}Cd_xS$ samples under irradiation with a 368 nm LED for 10 h, with the average H_2 evolution rates presented in Fig. 6b. The data obtained show a different trend: the H_2 evolution rate gradually decreases upon increasing the Cd molar fraction in the $Zn_{1-x}Cd_xS$ solid solution. The time courses of evolved H_2 for the two irradiation conditions are presented in Fig. S6.†

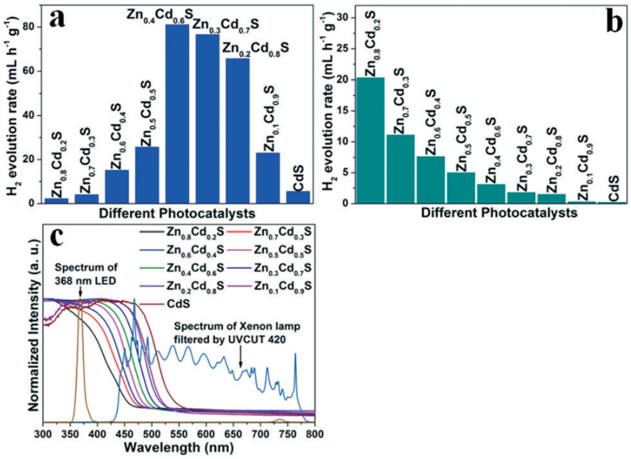

Fig. 6 Photocatalytic H_2 evolution rates of the powdered $Zn_{1-x}Cd_xS$ ($0.2 \leq x \leq 1$) samples dispersed in Na_2S/Na_2SO_3 aqueous solution under (a) visible-light irradiation with a Xe lamp filtered by a UVCUT 420 ($\lambda \geq 420$ nm) and (b) 368 nm LED irradiation. (c) The normalized UV-vis diffuse reflectance spectra of $Zn_{1-x}Cd_xS$ overlaid with the normalized light spectra profiles of the 368 nm LED and the Xe lamp filtered by a UVCUT 420.

The photocatalytic activity of solid state semiconductor photocatalysts can be relevant to their crystallinity,[32] light absorption,[3] surface area,[33] absolute valence/conduction band positions,[34–36] and the lifetime of photo-excited carriers.[37,38] For the samples reported here, $Zn_{0.4}Cd_{0.6}S$ has been most efficient in terms of hydrogen generation under irradiation by visible light, while it had rather poor crystallinity as judged by the lower signal intensity of the (002) main peak in Fig. 1. In terms of the PL lifetimes, all $Zn_{1-x}Cd_xS$ samples are rather similar (Fig. 5b). The light absorption by $Zn_{1-x}Cd_xS$ ($0.2 \leq x \leq 1$) samples is displayed in Fig. 6c in order to demonstrate that all the samples can absorb the light emission of a 368 nm LED, while an increasing fraction of the visible light from the cut-off spectra of the Xe lamp becomes absorbed by the samples with a larger Cd content. We recall here that $Zn_{0.4}Cd_{0.6}S$ samples show the best photocatalytic activity under visible-light irradiation (Fig. 6a), but it is not the most efficient visible light absorber according to Fig. 6c. In order to exclude the influence of surface area on the photocatalytic performance for H_2 production, the H_2-production rates per unit area of the samples are shown in Table S1† based on the same incident light irradiation (368 nm LED as the light source). The values gradually decrease with increasing Cd content. It means that the surface area is not the main factor for the different photocatalytic activities in this work. It is well established that the absolute positions of the conduction and valence bands continuously shift upon the opening of the optical band gap with increasing Zn content in the $Zn_{1-x}Cd_xS$ solid solution (see calculated values above). Under the conditions of irradiation by a 368 nm LED (Fig. 6b), it is the $Zn_{0.8}Cd_{0.2}S$ sample with the highest conduction and the lowest valence band positions which exhibits the best photocatalytic activity, resulting from the stronger redox ability of the photo-excited electrons and holes.[34–36] Fig. 6b points out at the same time that the band positions of $Zn_{0.4}Cd_{0.6}S$ are not the most favourable ones for the redox reaction in photocatalytic water splitting. We thus conclude that it is a balance between the light absorption and the redox activity due to the appropriate absolute band positions which results in the most efficient photocatalytic activity of $Zn_{0.4}Cd_{0.6}S$ under visible-light irradiation in this work.

7. Conclusions

In summary, a series of hexagonal $Zn_{1-x}Cd_xS$ powdered photocatalysts with variable composition ($0.2 \leq x \leq 1$) confirmed by ICP-AES has been successfully synthesized by a solvothermal method. The XPS spectra of Zn 2p and Cd 3d regularly shift upon changing the composition of the $Zn_{1-x}Cd_xS$ samples, due to the difference in the Mulliken atomic charges of Zn, Cd, and S. The photocatalytic activity of $Zn_{1-x}Cd_xS$ samples in terms of hydrogen generation from water has been evaluated under visible-light irradiation ($\lambda \geq 420$ nm) and with a 368 nm LED. The $Zn_{0.4}Cd_{0.6}S$ sample exhibited the highest photocatalytic H_2 evolution rate (81 mL h^{-1} g^{-1}) under visible-light irradiation, while for the UV LED irradiation, the H_2 evolution rate gradually decreased with increasing Cd fraction in the $Zn_{1-x}Cd_xS$ solid solutions. By comparing the crystallinity, surface area, valence/conduction band positions, absorption spectra and fluorescence lifetimes, we conclude that the photocatalytic activity is related to the balance between the absolute positions of the valence/conduction bands and the light absorption ability of the $Zn_{1-x}Cd_xS$ photocatalysts.

Acknowledgements

The authors acknowledge the financial support from the National Project for EV Batteries (20121110, OptimumNano, Shenzhen), the Guangdong Innovation Team Project (no. 2013N080), and The Hong Kong Scholar Program (XJ2014046).

Notes and references

1 K. Chang, Z. Mei, T. Wang, Q. Kang, S. Ouyang and J. Ye, *ACS Nano*, 2014, **8**, 7078–7087.
2 K. Chang, M. Li, T. Wang, S. Ouyang, P. Li, L. Liu and J. Ye, *Adv. Energy Mater.*, 2015, **5**, 1402279.
3 Z. Mei, B. Zhang, J. Zheng, S. Yuan, Z. Zhuo, X. Meng, Z. Chen, K. Amine, W. Yang, L.-W. Wang, W. Wang, S. Wang, Q. Gong, J. Li, F.-S. Liu and F. Pan, *Nano Energy*, 2016, **26**, 405–416.
4 J. Zhang and X. Wang, *Angew. Chem., Int. Ed.*, 2015, **54**, 7230–7232.
5 C. Pan, T. Takata, M. Nakabayashi, T. Matsumoto, N. Shibata, Y. Ikuhara and K. Domen, *Angew. Chem., Int. Ed.*, 2015, **54**, 2955–2959.
6 H. Ahmad, S. K. Kamarudin, L. J. Minggu and M. Kassim, *Renewable Sustainable Energy Rev.*, 2015, **43**, 599–610.
7 Z. Mei, S. Ouyang, D.-M. Tang, T. Kako, D. Golberg and J. Ye, *Dalton Trans.*, 2013, **42**, 2687–2690.

8 X. Chen, S. Shen, L. Guo and S. S. Mao, *Chem. Rev.*, 2010, **110**, 6503–6570.

9 J. F. Reber and M. Rusek, *J. Phys. Chem.*, 1986, **90**, 824–834.

10 M. Li, J. Jiang and L. Guo, *Int. J. Hydrogen Energy*, 2010, **35**, 7036–7042.

11 K. Zhang, D. Jing, C. Xing and L. Guo, *Int. J. Hydrogen Energy*, 2007, **32**, 4685–4691.

12 C. Xing, Y. Zhang, W. Yan and L. Guo, *Int. J. Hydrogen Energy*, 2006, **31**, 2018–2024.

13 M. Liu, L. Wang, G. Lu, X. Yao and L. Guo, *Energy Environ. Sci.*, 2011, **4**, 1372–1378.

14 Q. Li, H. Meng, P. Zhou, Y. Zheng, J. Wang, J. Yu and J. Gong, *ACS Catal.*, 2013, **3**, 882–889.

15 Y. Wang, J. Wu, J. Zheng and R. Xu, *Catal. Sci. Technol.*, 2011, **1**, 940–947.

16 J. Shi, H. Cui, Z. Liang, X. Lu, Y. Tong, C. Su and H. Liu, *Energy Environ. Sci.*, 2011, **4**, 466–470.

17 F. del Valle, A. Ishikawa, K. Domen, J. A. Villoria de la Mano, M. C. Sánchez-Sánchez, I. D. González, S. Herreras, N. Mota, M. E. Rivas, M. C. Álvarez Galván, J. L. G. Fierro and R. M. Navarro, *Catal. Today*, 2009, **143**, 51–56.

18 L. Wang, W. Wang, M. Shang, W. Yin, S. Sun and L. Zhang, *Int. J. Hydrogen Energy*, 2010, **35**, 19–25.

19 D.-H. Wang, L. Wang and A.-W. Xu, *Nanoscale*, 2012, **4**, 2046–2053.

20 C.-C. Chan, C.-C. Chang, C.-H. Hsu, Y.-C. Weng, K.-Y. Chen, H.-H. Lin, W.-C. Huang and S.-F. Cheng, *Int. J. Hydrogen Energy*, 2014, **39**, 1630–1639.

21 J. Zhang, J. Yu, M. Jaroniec and J. R. Gong, *Nano Lett.*, 2012, **12**, 4584–4589.

22 Y. T. Lu, D. D. Wang, P. Yang, Y. K. Du and C. Lu, *Catal. Sci. Technol.*, 2014, **4**, 2650–2657.

23 Q. Li, H. Meng, J. Yu, W. Xiao, Y. Zheng and J. Wang, *Chem. – Eur. J.*, 2014, **20**, 1176–1185.

24 M. Nguyen, P. D. Tran, S. S. Pramana, R. L. Lee, S. K. Batabyal, N. Mathews, L. H. Wong and M. Graetzel, *Nanoscale*, 2013, **5**, 1479–1482.

25 J. Yu, J. Zhang and M. Jaroniec, *Green Chem.*, 2010, **12**, 1611–1614.

26 J. Zhang, L. Qi, J. Ran, J. Yu and S. Z. Qiao, *Adv. Energy Mater.*, 2014, **4**, 1301925.

27 Y. Wang, J. Wu, J. Zheng, R. Jiang and R. Xu, *Catal. Sci. Technol.*, 2012, **2**, 581–588.

28 Y.-G. Yu, G. Chen, L.-X. Hao, Y.-S. Zhou, Y. Wang, J. Pei, J.-X. Sun and Z.-H. Han, *Chem. Commun.*, 2013, **49**, 10142–10144.

29 H. J. Monkhorst and J. D. Pack, *Phys. Rev. B: Solid State*, 1976, **13**, 5188–5192.

30 J. P. Perdew and Y. Wang, *Phys. Rev. B: Condens. Matter Mater. Phys.*, 1992, **45**, 13244–13249.

31 Z. Mei, S. Ouyang, Y. Zhang and T. Kako, *RSC Adv.*, 2013, **3**, 10654–10657.

32 M. Hojamberdiev, K. Yubuta, J. J. M. Vequizo, A. Yamakata, S. Oishi, K. Domen and K. Teshima, *Cryst. Growth Des.*, 2015, **15**, 4663–4671.

33 N. Zhang, S. Ouyang, T. Kako and J. Ye, *Chem. Commun.*, 2012, **48**, 1269–1271.

34 M. Manikandan, T. Tanabe, P. Li, S. Ueda, G. V. Ramesh, R. Kodiyath, J. Wang, T. Hara, A. Dakshanamoorthy, S. Ishihara, K. Ariga, J. Ye, N. Umezawa and H. Abe, *ACS Appl. Mater. Interfaces*, 2014, **6**, 3790–3793.

35 N. Zhang, C. Chen, Z. Mei, X. Liu, X. Qu, Y. Li, S. Li, W. Qi, Y. Zhang, J. Ye, V. A. L. Roy and R. Ma, *ACS Appl. Mater. Interfaces*, 2016, **8**, 10367–10374.

36 M. Zhao, H. Xu, H. Chen, S. Ouyang, N. Umezawa, D. Wang and J. Ye, *J. Mater. Chem. A*, 2015, **3**, 2331–2337.

37 W. Zhen, J. Ma and G. Lu, *Appl. Catal., B*, 2016, **190**, 12–25.

38 Q. Liu, T. Chen, Y. Guo, Z. Zhang and X. Fang, *Appl. Catal., B*, 2016, **193**, 248–258.